On the use of filament-based free wake panel methods for preliminary design of propeller-wing configurations

Ribeiro, André F.P.; Ferreira, Carlos; Casalino, Damiano

Important note
To cite this publication, please use the final published version (if applicable).
Please check the document version above.

On the use of filament-based free wake panel methods for preliminary design of propeller-wing configurations

André F.P. Ribeiro *, Carlos Ferreira, Damiano Casalino

Faculty of Aerospace Engineering, Delft University of Technology, Kluyverweg 1, Delft, 2629 HS, Netherlands

ARTICLE INFO

ABSTRACT

With distributed propulsion and electric vertical take-off and landing aircraft on the rise, fast and accurate methods to simulate propeller slipstreams and their interaction with aircraft components are needed. In this work, we compare results obtained with a filament-based free wake panel method to experimental and previously validated numerical data. In particular, we study a propeller-wing configuration at zero angle of attack and the aerodynamics of the blade-resolved slipstream interaction with the wing. We use a prescribed wake on the wing and a free wake on the propeller, which greatly accelerate the computations. Results indicate that, while forces are overpredicted due to the inviscid nature of the panel method, the free wake is able to capture the slipstream deformation and shearing with remarkable success. We find that a filament-based free wake panel method can be a useful tool for propeller-wing interaction in preliminary aircraft design.

1. Introduction

Aircraft design is currently undergoing a paradigm shift. While most aircraft flying today follow the classic tube and wing concept, with wing or tail-mounted turbofans or front-mounted propellers, the vast majority of aircraft being designed are for the electric vertical take-off and landing (eVTOL) market, where configurations are more varied and less traditional. These configurations are blurring the lines between rotorcraft and aircraft, usually with several propellers that have slipstreams going over the wings, fuselage, and tail. For flight mechanics and noise, the trajectories of these slipstreams and their interactions with other rotating and non-rotating components are critical. In parallel, aircraft with distributed propulsion, where a large number of propellers are mounted on the wing, are also being designed and studied [1]. Such wings require a deeper integration of the propulsion and wing during design than traditional aircraft, as a much larger portion of the wing is inside slipstreams.

Many experimental studies are being conducted on propellers with a focus on eVTOL and distributed propulsion [2–5]. These help understand the physics involved in these new configurations, while providing validation data for numerical studies [6] using computational fluid dynamics (CFD), which can then be applied to aircraft design and analysis. An alternative to lattice-Boltzmann method (LBM) and Navier-Stokes simulations of these aircraft is to use vortex methods [7], which allow

for blade resolved simulations of propellers, wings, and their wakes. With the complex physics of slipstream-wing interaction, some research is being done on using the vortex particle method approach to the wakes [8,9]. These methods can accurately predict many physical aspects of wakes, including leapfrogging and vortex breakup [10].

A more traditional approach to simulating wakes in potential flow is to use panel-based or filament-based wakes [11]. Such approach is less accurate than particle-based methods for wake-body interactions, but it is also simpler to implement and requires fewer equations to be solved. Filament-based wakes have been heavily used over the past 60 years to simulate steady cases for aircraft [12] and unsteady cases for rotorcraft [13–16]. However, their use for complex eVTOL configurations has been more limited [17]. In particular, studies verifying the feasibility of this method for propeller-wing interactions are not common and, to the authors knowledge, no detailed attempt at validating these methods with experimental data on slipstream deformation has been made.

In this work, we make use of experimental [5] and validated high-fidelity simulation data [6] of a propeller-wing interaction case to investigate the potential use of a filament-based free wake panel method for preliminary design of aircraft with complex slipstream interactions. We use an inviscid panel method to model the wing and propeller surfaces directly. Our focus is on understanding the accuracy of such a

---

* Corresponding author.
  E-mail address: andre.ribeiro@3ds.com (A.F.P. Ribeiro).

method and its limitations in assessing the aerodynamic characteristics of propeller-wing configurations.

2. Numerical methods

In this section, we provide a brief description of the numerical methods used herein. For more details on these methods and the implementations used in this work, we refer readers to the cited papers.

2.1. Lattice-Boltzmann method

The LBM [18] is a CFD approach that is based on a discrete form of the Boltzmann equation. Due to its numerical simplicity, it is able to perform unsteady simulations at a fraction of the time of traditional Navier-Stokes solvers [19]. Our LBM computations are conducted with PowerFLOW®, a commercial CFD code. It employs a $k - \epsilon$ RNG turbulence model [20] with a swirl model [21], which reduces the eddy viscosity in the presence of resolved flow structures, an approach called very large eddy simulation (VLES). A unique capability of PowerFLOW is in the handling of very complex geometries [22], with its Cartesian mesh being cut by surface elements, or surfels [23]. A sliding mesh [24] is used to rotate the propeller. Validations of the approach used here that are relevant to this work include vortical flows [25], rotors [26–32], and a propeller-mounted high-lift wing [33]. Details on the method and a full validation for the case investigated here can be found in [6].

2.2. Free wake panel method

We employ a source and doublet panel method with free wake modeling [11]. The code employed in this work was recently validated for moving airfoils and wind turbine rotors [34], including several dynamic effects [35] and aeroelasticity [36]. The thickness effects are fully captured, as the triangular or quadrilateral panels lie on the aircraft surfaces. The method uses a boundary element approach, with each surface panel and wake filament influencing all the others [37], meaning no volume mesh is needed.

Assuming incompressible, irrotational, inviscid flow, one can define a velocity potential Φ such that $\vec{u} = -\nabla\Phi$, where $\vec{u}$ is the flow velocity. By applying Green's theorem to this velocity potential equation, we can arrive at [11]:

$$\frac{1}{4\pi} A_{ij}\mu_j + \frac{1}{4\pi} B_{ij}\sigma_j + \frac{1}{4\pi} C_{iw}\gamma_w = 0 \tag{1}$$

where μ is the doublet strength on solid surfaces, σ is the source strength on solid surfaces, γ is the vortex ring strength on wake panels (which is equivalent to doublet wake panels [11]), A_{ij} and B_{ij} are elements of square matrices containing the influence coefficients of surface panel j on surface panel i, and C_{iw} is composed of the influence of the wake panel w on surface panel i. The influence coefficients represent the velocity potential field around a panel and are purely geometric and depend on the relative position of the two panels in question. A representation of the velocity potential field created by source and doublet panels and the associated streamlines is shown in Fig. 1. We use influence formulations that are independent of local coordinate systems [37].

A common way to close Eq. (1) is to set σ and γ, while leaving μ as the only unknowns. The source strengths are defined in a way to enforce surface impermeability, using:

$$\sigma = -(\vec{U}_\infty - \vec{u}_{body}) \cdot \hat{n} \tag{2}$$

where $\vec{U}_\infty$ is the freestream velocity, $\vec{u}_{body}$ is the kinematic velocity of the surface panel itself and $\hat{n}$ is the unit vector normal to the panel. The strength of the wake vortex rings can be calculated as the jump in potential over the trailing edge, which enforces the Kutta condition. This is computed based on the potential of the adjacent top and bottom

panels, including $\Phi_\infty = \vec{U}_\infty \cdot \vec{x}$, which is the freestream potential at an arbitrary location $\vec{x}$. The Kutta condition is hence [38]:

$$\gamma = \mu_{top} - \mu_{bottom} - (\Phi_{\infty top} - \Phi_{\infty bottom}) \tag{3}$$

Traditional free wake panel methods have issues with singularities when wakes intersect solid bodies. This happens due to divisions by zero in the equations for the influence coefficients. One way to avoid this issue is by changing the formulation of the wake panels from velocity potential to velocity panels [14]. The different kind of panels are illustrated in Fig. 2.

The first row of wake panels after the trailing edge is dealt with by adding their influence coefficients C_{iw} to A_{ij}. After the system is solved, γ is computed with Eq. (3) and is preserved in the corresponding wake panel for the remainder of the simulation. The next few wake panels rows (the exact number is a user input) are dealt with by calculating C_{iw}, multiplying it by γ_w and subtracting it from the right hand side of the linear system of equations. This is known as the near wake. The subsequent panels are in the far wake and instead of computing their contribution to the velocity potential $C_{iw}\gamma$, we use the Biot-Savart equation to compute the contribution of each wake filament to the velocity of each surface panel. This equation leads to singularities when the velocity is computed very close to the wake filaments. This is illustrated in Fig. 3, where the purely inviscid solution is shown in black and the velocity u_i induced by the vortex tends to infinity as the distance x goes to zero. The singularities can then be avoided by using a vortex core model, which reduces the velocities induced by the wake filaments to zero on the filaments themselves. The particular vortex core model we use in this work [39] is Reynolds number and γ dependent. A few examples of how the singularities are avoided are shown in Fig. 3, where r is the vortex radius, which grows with time and is affected by vortex stretching [39].

With the total velocity induced by all the far wake filaments on a given surface panel $\vec{u}_{fw}$, we can then enforce surface impermeability by adding this additional velocity to Eq. (2):

$$\sigma = -(\vec{U}_\infty + \vec{u}_{fw} - \vec{u}_{body}) \cdot \hat{n} \tag{4}$$

The new values of σ can then be multiplied by their influence coefficients and $B_{ij}\sigma_j$ can be subtracted from the right hand side of the linear system of equations. Hence, the near wake affects the left hand side of the linear system in Eq. (1) and the far wake affects the right hand side. This stabilizes the problem and allows for cases of strong wake-body interaction to be computed. The linear system can then be solved with the generalized minimal residual method (GMRES). For this work, we use the lower-upper (LU) decomposition of the left hand side matrix in an early timestep as a preconditioner for all subsequent timesteps, which accelerates GMRES by an order of magnitude.

Velocities on the surface are computed based on the gradient of the surface potential μ with central differences for quadrangular panels, but a least squares approximation [40,41] is also available, and is always used for triangular panels. With the surface velocity available, the unsteady Bernoulli equation is used to find the surface pressure, which is then integrated over all surface panels to find the forces and moments acting on the bodies. The unsteady Bernoulli equation for potential flows including arbitrary motions is [42]:

$$\frac{p - p_\infty}{\rho} = -\frac{\left\|\vec{u}_p\right\|^2}{2} + (\vec{u}_{body} - \vec{U}_\infty) \cdot (\vec{u}_p) + \frac{\partial\mu}{\partial t} \tag{5}$$

where p is the instantaneous pressure in a given panel, p_∞ is the freestream pressure, ρ is the fluid density, and $\vec{u}_p$ is the perturbation velocity caused by the sources and doublets [37]. When the far wake treatment is added, the unsteady Bernoulli equation requires additional terms [15]:

$$\frac{p - p_\infty}{\rho} = -\frac{\left\|\vec{u}_p + \vec{u}_{fw}\right\|^2}{2} + (\vec{u}_{body} - \vec{U}_\infty) \cdot (\vec{u}_p + \vec{u}_{fw})$$

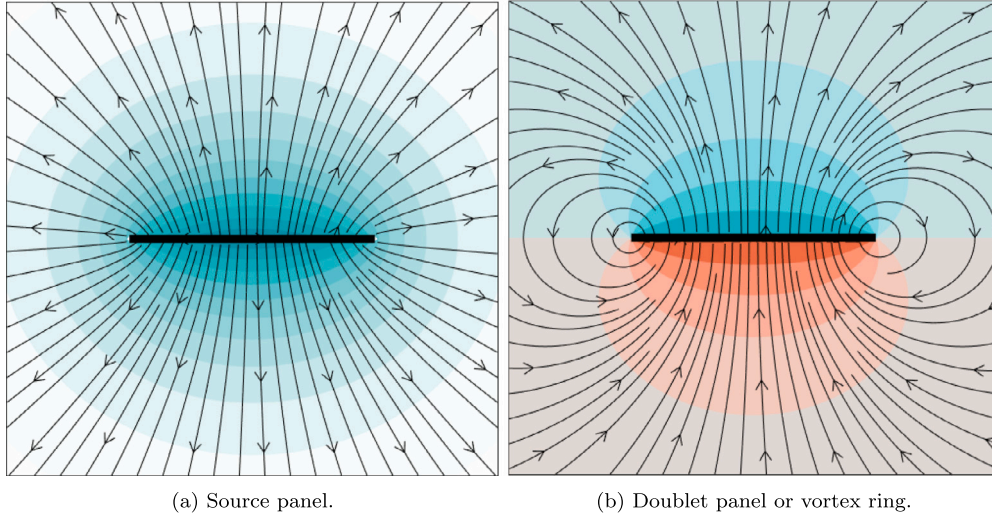(a) Source panel.

(b) Doublet panel or vortex ring.

Fig. 1. Contour on center plane square panels showing velocity potential created by the panels and associated streamlines.
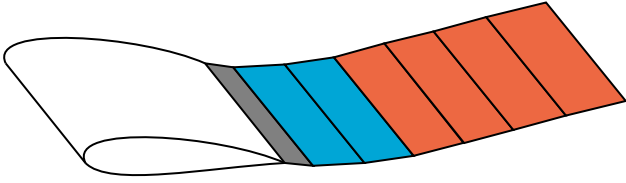

Fig. 2. The three types of wake panels behind an airfoil. The first row after the trailing edge, in grey, is the row of the "Kutta panels", where the Kutta condition of Eq. (3) must be fulfilled. The near wake panels are in blue, and the far wake panels, where the novel formulation of [14] is applied, are in orange. (For interpretation of the colors in the figure(s), the reader is referred to the web version of this article.)
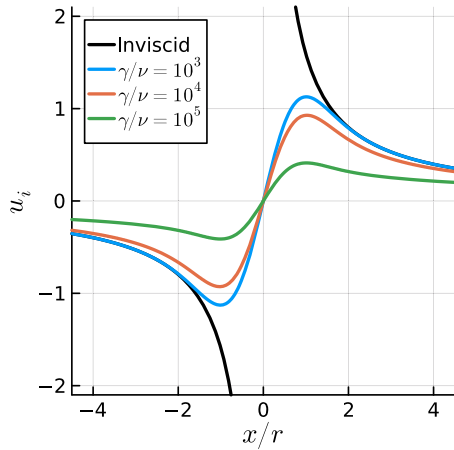

Fig. 3. Velocity induced by a unit vortex along a line going through its center.

$$+ \frac{\partial \mu}{\partial t} - \frac{\partial \phi_{fw}}{\partial t} \qquad (6)$$

where the velocity induced by the far wake $\vec{u}_{fw}$ needs to be added to the perturbation velocity $\vec{u}_p$ and the time derivative of the potential induced by the far wake ϕ_{fw} needs to be included. This time derivative is composed of three terms: one related to the wake velocity, one related to the wake deformation, and one related to the flux of wake points through the near wake/far wake boundary. The second term can usually be neglected [15], leading to:

$$\frac{\partial \phi_{fw}}{\partial t} = \sum_{w=1}^{N_{fw}} (\vec{u}_{body} - \vec{w}_w) \cdot \vec{u}_{fw,w} - \sum_{w=1}^{N_{TE}} C_{w,1} \gamma_w \qquad (7)$$

where N_{fw} is the number of far wake panels, $\vec{w}_w$ is the velocity of wake panel w, and $\vec{u}_{fw,w}$ is the velocity induced by the far wake panel w on the surface panel where p is being computed. The last term is a line integral of the induced potential of the first filament of the first far wake panel (i.e., the filament shared with the last near wake panel). Hence, it is integrated over a number of filaments equal to the number of trailing edge filaments on the bodies (N_{TE}). During testing, this term seemed to play a negligible role in pressure, but its computation is also very quick in comparison to the wake velocity term.

3. Test case description

The geometry used in this work is a straight wing based on the NLF-Mod22(B) airfoil [43], with a nested chord $c = 300$ mm, a span of 1.248 m. We focus on results at an angle of attack of 0° and nested flap (i.e. the flap is not deployed). The wing is equipped with a TUD-XPROP-S reference propeller [4,44], with 6 blades, diameter $D = 203.2$ mm, and a blade pitch at 70% of the radius of 30°. The propeller is installed 173.5 mm ($\approx 0.858D$) ahead of the leading-edge, with the axis of rotation angled 5° with respect to the wing chord line. The flow conditions are freestream velocity $U_\infty = 30$ m/s, resulting in a wing chord Reynolds number $Re \approx 600,000$, a freestream Mach number $M \approx 0.09$, and a propeller advance ratio of $J = U_\infty/(Dn) = 0.8$, where n is the rotational speed in rotations per second. A view of the geometry is shown in Fig. 4, where the planes where surface pressure were measured are also highlighted.

3.1. Numerical setup - Lattice-Boltzmann

Simulations are run with PowerFLOW 6-2021-R7, using the subsonic isothermal solver, as the blade tip Mach number due to the propeller rotation is 0.35. A Cartesian mesh is used, with cubic cells ranging from 0.03 mm on the propeller blades leading-edges to 61 mm far from the wing. An average y^+ of 40 was used on the wing, which is compatible with the wall function used. The simulations are similar in setup to previous works on wing sections [45,46]. The wind tunnel walls are included to account for blockage effects, but are simulated as free slip walls. The surfaces of the propeller and wing are modeled as fully turbulent. The boundary conditions used in the upstream and downwind faces of the numerical wind tunnel are a velocity inlet and a pressure outlet, respectively. More details on the setup can be found in
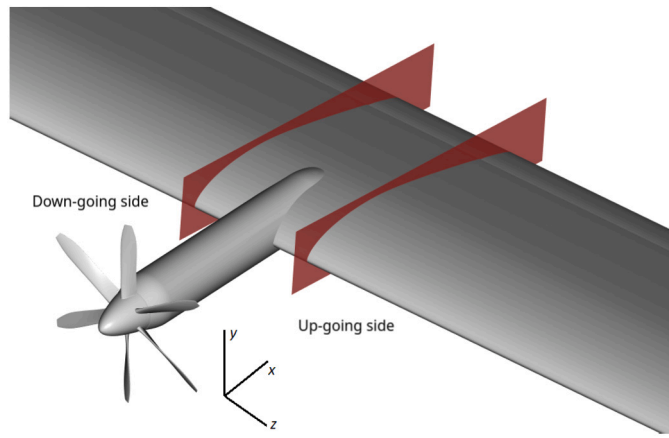
Fig. 4. Geometry of the simulated propeller and wing. Red planes are where surface pressure was measured. Up and down-going refer to the direction of the propeller rotation. Coordinate system used throughout the work also shown.

[6], where a resolution study and validation with experimental data are available.

3.2. Numerical setup - free wake panel method

The panel code used in this work can handle surface meshes composed of triangles and quads, which means that including the propeller nacelle, boom, and pylon is not difficult. However, as this study focuses on using this method for preliminary design, we remove these components for simplicity and simulate floating blades spinning in front of the wing. This is common practice for vortex lattice methods [47], due to limitations of such methods, but also for panel codes [17] for simplicity. This is illustrated in Fig. 5, where the detailed geometry used in the LBM simulation is compared to the surface mesh used by the panel method.

The wing itself is also simplified for the panel code, with the removal of the gap between the main element and the flap, along with the flap brackets. Another simplification is that in the free wake formulation used here, trailing-edges must be sharp. Hence, sharp trailing-edges were used on the wing and blades. Finally, we changed the wing aspect ratio from about 4 to nearly 15. This was done because in the LBM simulations free slip boundary conditions were used on the sides of the numerical domain, which can be done with the panel method with symmetry conditions [11], but would add to the cost without substantially affecting the results. Hence, we simply extend the wing span to avoid strong effects from the tip vortices. As shown in Section 5.3, the outboard pressure distribution using both methods is very similar, indicating the different approaches to the wing tip are equivalent.

The wing is discretized with 150 panels along the chord with cosine spacing and 50 panels along span, with a spanwise spacing of about $c/40$ in slipstream, growing with a geometric progression to over $2c$ at the edges. The blades are discretized with 100 panels along chord with cosine spacing and 50 panels along the span, with constant spacing. The timestep was chosen to achieve a propeller rotation between 2.5 and 20° per timestep. The space and time discretizations were selected based on previous experience with the code [36,34], while attempting to keep simulation costs compatible with preliminary design, with the finer mesh on the wing chord (compared to the blades) being selected due to the wing leading-edge interaction with the propeller wake.

The vortex core model used an initial vortex age of $1/12n$, where n is the propeller rotation frequency. This corresponds to a vortex core radius of 0.45 mm at the propeller trailing-edge, or about 3% of the blade chord. As the propeller wake develops and the vortex cores grow, the vortex core radius of the filaments coming from the propeller are about 1.5 mm as they reach the wing trailing-edge. The standard con-

stants described in the original article for the vortex core model were used [39].

4. Wake discretization effects on isolated components

4.1. Wing wake

The timestep used in the free wake simulations is directly linked to the number of wake panels that must be calculated during the simulation. Every timestep a new row of wake panels is added to the wing and propeller blades. The timestep required for simulating a wing can be quite large, typically several times larger than a flow pass $t_w = c/U_\infty$, while rotors cannot have timesteps that would lead to corresponding azimuthal rotations $\Delta \psi$ that are excessive. Hence, we have a conflict between the propeller rotation period $t_p = 1/n$ and t_w. In the case of the present simulations, to achieve a $\Delta \psi$ of about 20°, we require the timestep to correspond to $t_w/33$.

For the forces on the wing to converge to a steady state solution, the startup vortex (i.e., the last filament in the wake) needs to convect to a large distance, $O(10c)$ or even $O(100c)$. This means that the simulation with the propeller resolved at $\Delta \psi = 20°$ requires hundreds of timesteps, increasing the cost dramatically, as calculating the wake self induction is an N^2 problem.

A different issue with the wake that appeared in our simulations was due to the far wake formulation. In order for the propeller wake panels to switch to the far wake formulation before impinging on the wing leading-edge, we start using such formulation after about $\Delta \psi = 200°$, or 10 wake rows when $\Delta \psi = 20°$. From the blade airfoil sections point of view, this is a substantial distance, but from the wing point of view, this means the far wake formulation starts on the wing wake after a distance of about $c/3$. Hence, the wing far wake formulation starts close to its trailing-edge, leading to inaccurate results.

One possible solution to the problem of the far wake formulation being used too close to the wing trailing-edge would be to change the code to allow for different wakes to use different formulations, i.e. using the far wake formulation on the propeller only. This would solve this problem, but would still leave us with the issue of the long time required to converge the forces on the wings.

Hence, we use a different approach that solves both problems concurrently: we employ a prescribed wake for the wing and a free wake for the propeller. Wake panels on the wing still appear at every timestep, but they are forced to be aligned with the freestream and are stretched to an arbitrary length of 1 m. This is done for all wake panels, regardless of the formulation (see Fig. 2). Hence, the wing wake quickly becomes very long, moving the startup vortex away, while also making the far wake formulation only take place after a distance of more than $30c$. The assumptions here are that the wing is converging to a steady circulation, meaning the unsteady effects of vortex strengths being created at the trailing-edge are negligible. This was verified with a purely free wake simulation, where we observe that at the wing tips the wing circulation is converging to steady results and behind the propeller the fluctuations in circulation are around ±1%.

The impact of the distance between the start of the far wake and the wing trailing-edge (fw_s), the timestep (Δt), and the use of the prescribed wake on the lift coefficient ($C_L = F_y/(q_\infty cS)$, where F_Y is the force in the vertical direction, $q_\infty = 0.5\rho_\infty U_\infty^2$ is the freestream dynamic pressure, ρ_∞ is the freestream air density, and S is the wing span) are shown in Fig. 6. The blue, orange, and green lines show that reducing fw_s can have an effect on C_L, as when $fw_s = 3c$, C_L is reduced by a small amount (about 0.2%), while the effect at $fw_s = 1c$ is about four times larger. As mentioned previously, with the propeller in place, $fw_s = c/3$, which would lead to even larger errors. We can also see in Fig. 6 the effect of increasing Δt, by comparing the blue and purple lines. An increased timestep is very advantageous for the computational cost, as we can observe much fewer iterations are needed for C_L to stabilize when a larger timestep is used. Finally, the prescribed wake

(a) Geometry used in LBM simulation.

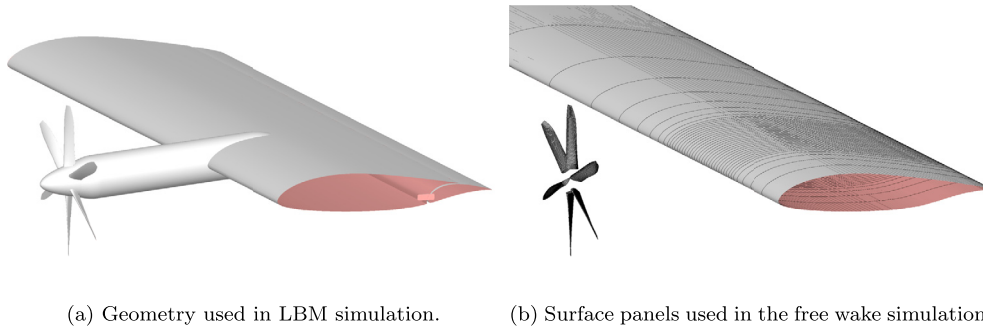(b) Surface panels used in the free wake simulations.

Fig. 5. Geometries used for the two numerical methods. Clip plane present on the port side, to visualize the flap gap and bracket on the LBM model.
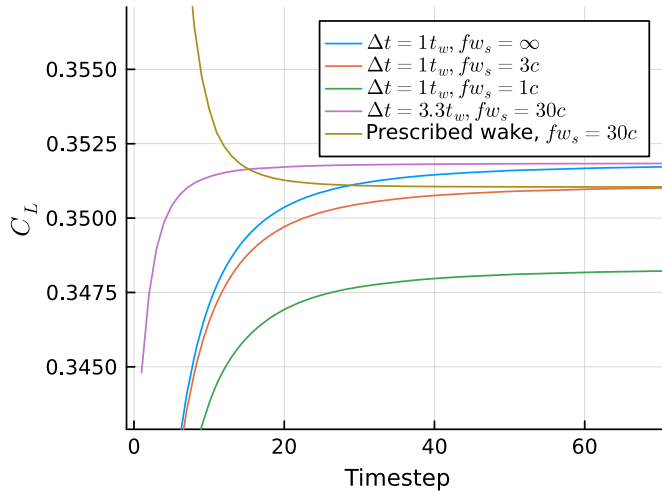

Fig. 6. Effect of far wake start distance, timestep length, and prescribed wake on the lift coefficient of the standalone wing.

results are also shown, in gold. While the results do not match the blue and purple lines perfectly, the difference is small (again about 0.2%), and the number of iterations required to reach convergence is similar to using a large timestep. Hence, the prescribed wake for the wing is the approach we choose for the simulations in this work, solving the problems of the near wake effects and the slow convergence due to the small timestep required by the propeller concurrently.

4.2. Propeller wake

As mentioned before, the timestep for the propeller is more stringent than that of the wing and ultimately drives the simulation cost. Here, we simulate the isolated propeller aligned with the freestream, which can be done with six-fold axisymmetry, meaning we only simulate one blade. We measure the thrust coefficient $T_c = T/(q_\infty A)$ and the torque coefficient $Q_c = Q/(q_\infty A R)$, where T is the thrust acting on the propeller, Q is the torque, $R = D/2$ is the propeller radius, and $A = \pi R^2$ is the propeller disk area. These coefficients can be compared with experimental values [4].

Results for the propeller are shown in Fig. 7. The timestep varies to obtain $\Delta\psi$ between 2.5 and 20°. The time is normalized in flow passes over the wing (which is not included here, but will be included later and understanding how many flow passes we need is important to estimate the cost of the simulations) and simulations are run for two flow passes, or 3.7 propeller rotations. The fact that the propeller forces converge in few flow passes is encouraging, regarding the convergence of the propeller-wing assembly, as it is an indicator that simulations will not have to run for a very long time. Two flow passes is nearly 70 timesteps for $\Delta\psi = 20°$, which, as shown in Fig. 6, is enough for the isolated wing to converge as well. The blue and orange lines indicate that the far wake

formulation works well for the propeller, as using it causes marginal changes in the thrust and torque. A grid convergent behavior can be seen for T_c and Q_c, with differences between the simulations becoming smaller as the timestep is decreased. The differences between $\Delta\psi = 5$ and 2.5° are under 0.5% and, hence, we consider $\Delta\psi = 5°$ a converged result. While T_c nearly matches experimental results for $\Delta\psi \le 5°$, Q_c is about 5% lower than the experiments for the same simulations, which is not surprising given that very accurate torque predictions require accurate sectional drag values, which the current inviscid method cannot achieve. Overall, we consider these results satisfactory for preliminary design.

5. Propeller-wing simulations results

5.1. Convergence

Fig. 8 shows the convergence of the total streamwise (F_x) and vertical (F_y) forces acting on the propeller-wing assembly, for each of the previously used values of $\Delta\psi$. Simulations use a prescribed wing wake unless stated otherwise. The prescribed wake on the wing leads to a fast and consistent force convergence of F_y, which is a major advantage over a full free wake approach. The timestep effects on F_x are very similar to the isolated propeller results, with $\Delta\psi = 5°$ appearing sufficient for grid convergence, from a mean force perspective. As $\Delta\psi$ is reduced, the unsteady effects of the propeller wake on the wing start becoming more apparent and higher frequencies are captured in the forces. After around 2 flow passes over the wing (which again, corresponds to 3.7 propeller rotations), the forces are statistically converged, whereas the full free wake approach requires about 25 flow passes. The peak in forces around $tU_\infty/c = 0.3$ corresponds to the propeller wake first reaching the wing leading-edge.

Fig. 9 illustrates the difference between the two wing wake approaches. On the left side, the full free wake approach is used and we can observe that all 200 rows of wake panels are very close together and still near the wing trailing-edge. On the right side, we see the prescribed wake approach on the wing combined with the free wake approach on the propeller. This forces the wing wake to move far from the trailing-edges very quickly, while still having a high resolution on the propeller, which as seen in Fig. 7, is necessary. Unless stated otherwise, for the remainder of this work "free wake simulations" refer to the mixed wake approach, with prescribed wing wake and free propeller wake.

5.2. Force development

Here, we focus on the forces acting on the wing sections along the span. Early XFOIL [48] simulations showed that the aerodynamic forces on the NLF-Mod22(B) airfoil are very sensitive to viscosity. For example, C_L in inviscid mode was nearly 70% higher than the one computed in viscous mode. Hence, we can expect that forces acting on the wing according to the inviscid free wake simulations are different from the LBM simulations. However, it would be useful if the effect of the propeller on the wing is captured in spite of these differences.
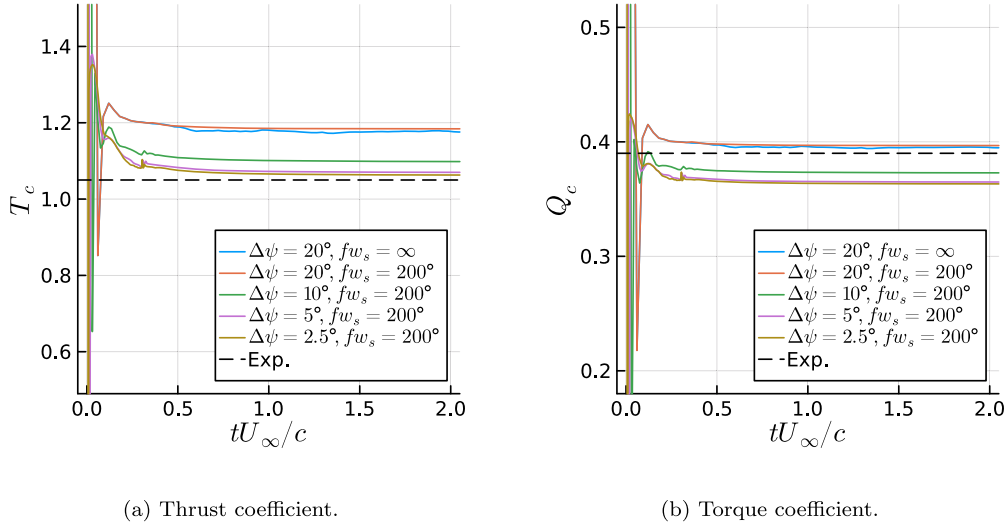
(a) Thrust coefficient.

(b) Torque coefficient.

Fig. 7. Time history of integral coefficients of the isolated propeller. Far wake and timestep effects.

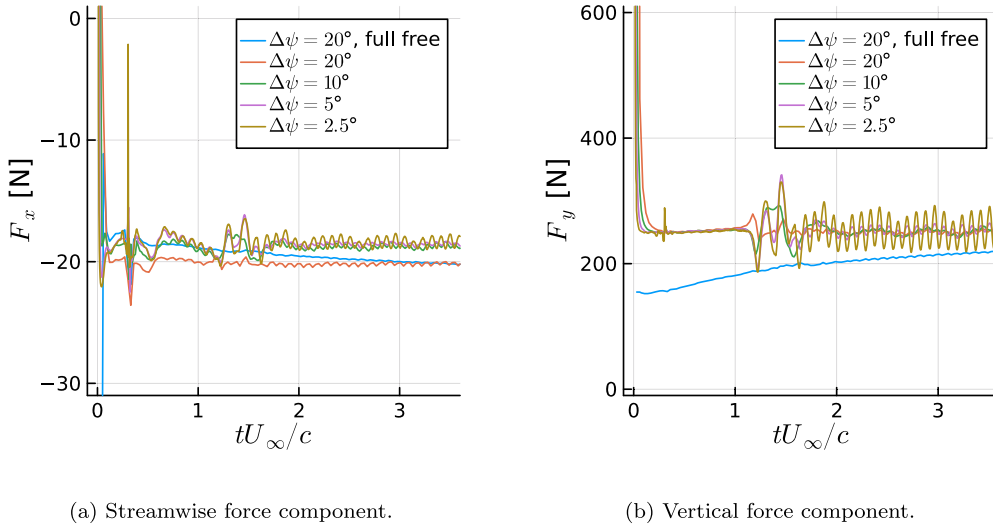(a) Streamwise force component.

(b) Vertical force component.

Fig. 8. Time history of forces on wing-propeller assembly. Perscribed wing wake and timestep effects.

We take spanwise sections of 16 mm from both the LBM and free wake simulations. Here we focus on $\Delta\psi = 5°$, as these are considered converged results, based on Section 5.1. The lift, drag ($C_D = F_x/(q_\infty cS)$), and pitching moment ($C_m = M/(q_\infty cSc)$, where M is the moment around the spanwise direction at the quarter chord location, with a positive value meaning nose up) coefficients along the wing span are shown in Fig. 10, where the forces and moments acting on the propeller are removed. Note that the LBM forces include the nacelle. For the results in this section, the reference span S is changed to the corresponding fraction of the wing span (16 mm), so that the development plots show quasi 2D results for each spanwise position. The orange and green lines show two possible approaches for correcting the inviscid data: shifting or scaling the curves. The values used for shifting and scaling are shown on the plots. For C_L, shifting the forces provides good agreement, but an overshoot of about 10% in the peak value, while scaling the forces make them match LBM data fairly well, with the down-going side (negative z) showing more discrepancies. For C_D both approaches are mostly inaccurate, due to the viscosity playing a large role in drag, i.e., as expected, drag forces obtained from an inviscid approach cannot be relied on. Shifting or scaling C_m seem to

produce reasonably good results on the down-going side ($z < 0$), but the trends on the up-going side are not captured.

5.3. Pressure distribution

Pressure coefficient $Cp = (p - p_\infty)/q_\infty$, where p is the static pressure and p_∞ is the freestream static pressure, is computed on two planes on each side (up-going and down-going) of the propeller axis, at 70% of the propeller radius (71.12 mm), as shown in Fig. 4. Pressure at these locations is available in the experimental data. We also select a plane further away from the slipstream, at $z/R = 3$, which is mostly outside of the effect of the slipstream as seen in Fig. 10. This plane serves to examine how the flow around the wing behaves without strong slipstream effects. The results are shown in Fig. 11.

We first focus on the Cp cut outside of the slipstream in Fig. 11a. Viscous and inviscid XFOIL results of the isolated wing section are also included. The XFOIL results assume no propeller effects. The viscous XFOIL results are very close to the LBM results, while the inviscid XFOIL data are very close to the free wake results, indicating that the small differences between the LBM and free wake simulations are mostly due
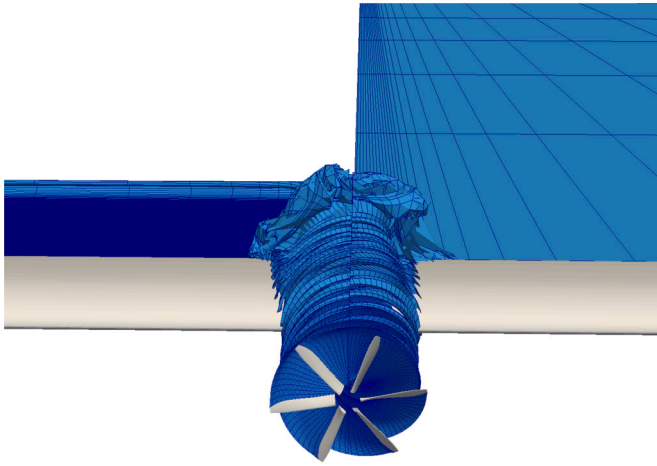
Fig. 9. Different wake approaches used in this work. Full free wake approach on the left, prescribed wake on the wing and free wake on the propeller on the right. Results after 200 timesteps, with $\Delta\psi = 5°$.

Table 1
Propeller thrust coefficient, along with 0.4 m span drag, lift, and moment coefficients.

	Exp.	LBM	Free Wake
T_c	1.05	1.04	1.10
C_D	-	0.025	0.054
C_L	-	0.32	0.41
C_m	-	-0.056	-0.078

to viscous boundary layer effects, in this plane. The viscous effects reduce the suction in the first three quarters of the chord and decrease the trailing edge pressure. The bump in the panel methods results near $x/c = 0.85$ is due to a discontinuity in the surface tangent on the suction side where the main element ends and the flap begins. The LBM simulation includes the actual flap gap, leading to a discontinuity in Cp. A similar effect appears in smaller magnitude on the pressure side near $x/c = 0.7$, where the pressure side flap gap is.

In the presence of the slipstream, in Figs. 11b and 11c, the results are qualitatively similar to the references, but as in Fig. 11a the trailing edge pressure is lower when viscosity is present. Over the entire airfoil, the slipstream seems to create more differences between the viscous and inviscid results. This is partially due to the propeller producing more thrust with the panel method, leading to higher total pressure and different wing section angle of attack. Another possible reason for the discrepancies is that the slipstream shearing is imperfect when using filament-based free wakes. We investigate this in Fig. 12, where we compare the experimental and LBM results at $z/R = \pm 0.7R$ to results obtained from the free wake simulations at $z/R = \pm 0.5R$. The agreement is excellent, indicating that the free wake-based slipstream has weaker shearing than in reality, which will be investigated more in Section 5.5.

5.4. Forces

We now look at the integrated forces on the propeller and wing in a quantitative manner. Table 1 shows the propeller thrust coefficient, and the lift, drag, and moment coefficients integrated over the wing. We compare the results obtained with the panel method (using $\Delta\psi = 5°$) with the LBM simulations and experiments. Integrated forces on the wings were not available from experiments. The wing forces are computed over an arbitrary span of 0.4 m, or about twice the propeller diameter.

The free wake results for T_c are less comparable to the reference values than they were for the case of the isolated propeller. The propeller is tilted with regards to the incoming free stream, which could lead to higher angles of attack along the blades, which tend to generate excess sectional lift with inviscid methods. The differences between the forces are substantial, as expected, due the large differences between viscous and inviscid XFOIL results for this wing. Hence, for practical use in preliminary design, corrections are needed.

5.5. Slipstream deformation

The previous sections showed some of the limitations of the inviscid free wake approach for forces and pressure on the wing and propeller. Away from the body, the viscous effects are expected to be smaller and the free wake approach is likely to be more accurate. The experimental campaign conducted for this propeller-wing configuration only included a total pressure plane at a distance of c downstream of the wing trailing-edge. In order to validate the free-wake method, including slipstream-wing interaction, we use the LBM results on planes at various streamwise locations. These planes are illustrated in Fig. 13.

In Fig. 14 and 15 we compare the numerical results for the planes shown in Fig. 13. In this section, we use $\Delta\psi = 2.5°$ to achieve maximum detail in the figures, although $\Delta\psi = 5°$ results are very similar. The figures show instantaneous (i.e., not time-averaged) velocity magnitude. At $x/c = 0.00$, we see very good agreement of the slipstream and stagnation region near the wing leading-edge. The main difference that can be observed in this and all subsequent planes is that the LBM results have sharper gradients, while the free wake results are more smeared. This is expected, as the LBM simulations are using a scale-resolving scheme, with a very fine space and time discretization, able to capture more complex and smaller flow structures than a free wake method.

As we move to $x/c = 0.25$, it is apparent that the free wake simulations create a velocity field inside the wing, which is not physically meaningful, but allows us to see an artefact of this method. Inside solid bodies, the flow velocity should be equal to the freestream in the formulation we use [37], but here the filaments from the propeller wake are crossing through the wing, inducing a velocity field. In order to correct for this, one would need to disable the filaments inside the bodies or cut the filaments as they pass over the wing. This would add cost and complexity to the code and could be implemented in the near future.

At $x/c = 0.50$ and $x/c = 0.75$, we see secondary flow structures forming on the far left and right sides, on the suction and pressure sides of the wing, respectively. Remarkably, the free wake is able to reproduce these flow structures to some extent. Even at $x/c \geq 1.00$ the shearing of the slipstream seems to be captured very well by the free wake simulations, in spite of the presence of the wing wake in this region, which is prescribed as flat. This indicates that the motion of the wing wake is not playing a large role in the near wake deformation. We can also observe that the geometry simplifications in the free wake simulations did not introduce major differences. Overall, the agreement between the free wake and LBM results is remarkable, both from a qualitative (shape of the slipstream) and quantitative (colors in the figures) point of view.

The 3D features of the slipstream are shown in Fig. 16. The breakup of the tip vortices in the LBM simulation can be seen at the top left of the image. The secondary vortical structure, where the slipstream edge touches the suction side of the wing, previously shown in the planes, can be seen in both simulations, with good agreement between them. The slipstream filaments from the free wake penetrating the wing can also be observed. Finally, the deformation of the tip vortices as they reach the wing leading-edge can also be seen in both simulations, although this deformation is more pronounced in LBM, as the free wake penetrates through the wing.

A close-up of the interaction between the propeller slipstream and wing leading-edge is shown in Fig. 17. In the free wake simulations, the velocity field induced by the wake filaments contributes to the
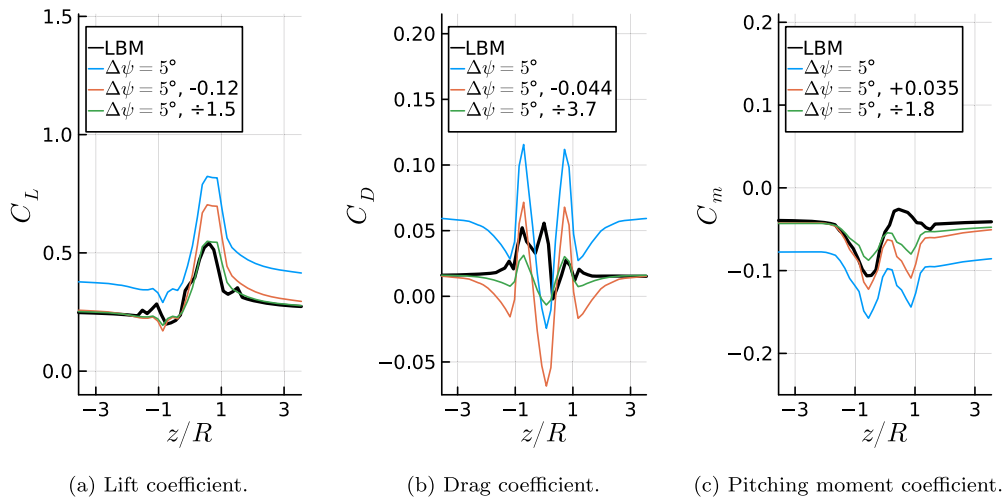
(a) Lift coefficient.

(b) Drag coefficient.

(c) Pitching moment coefficient.

Fig. 10. Wing force development along the span.

(a) Outside of slipstream

(b) Up-going side

(c) Down-going side

Fig. 11. Pressure coefficient along the wing chord.

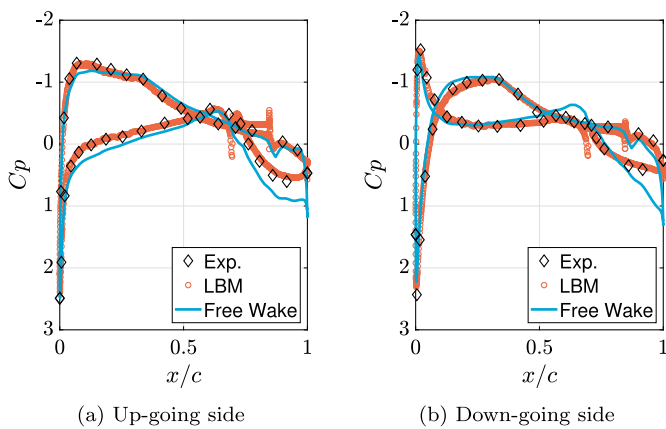(a) Up-going side

(b) Down-going side
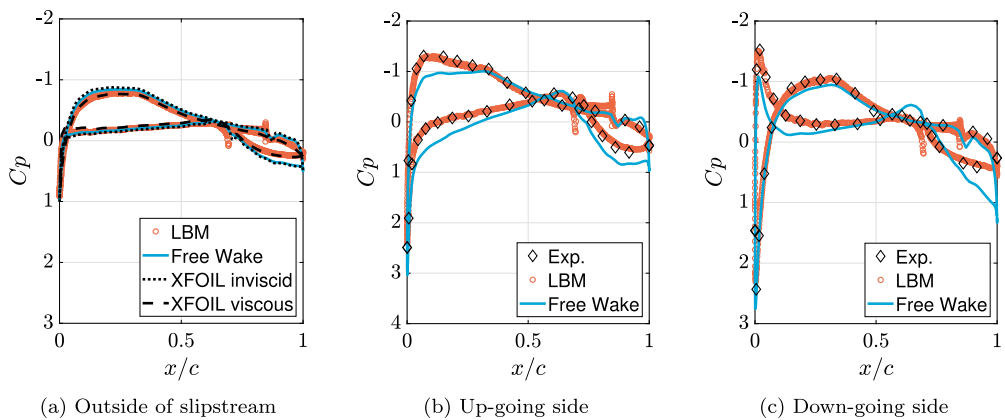
Fig. 12. Pressure coefficient along the wing chord. Experiments and LBM at $\pm0.7R$ of the center axis, results using the free wake approach at $\pm0.5R$.

sources on the wing surface, which attempt to enforce impermeability. However, in spite of the wake accumulating in front of the wing leading-edge at first, the finite timestep allows for filaments perpendicular to the wing to penetrate it. These filaments are highly stretched, as the wing sources attempt to push the wake nodes near the surface away from it, keeping most filaments parallel to the surface outside. The LBM results show that as impermeability is enforced, the tip vortices become extremely stretched over the leading-edge. In both cases, we can see the

tip vortices lagging behind near center of the suction side of the wing, meaning this effect is due to the leading-edge interaction with the vortices, not a viscous effect in the boundary layer. Inside the slipstream, we can also observe more complex 3D flow structures that form concentric cylinders around the propeller axis for both simulations. Again the similarities are remarkable. The most apparent shortcoming of the free wake simulation is the lack of vortex break-up, which is evident in the LBM results. The geometry simplifications clearly have some effect in the wakes of the blades roots, yet we believe a detailed design of the nacelle would require viscous effects to be accounted for and hence do not focus on this here.

5.6. Computational cost

The cost of each simulation used in this work is summarized in Table 2. Simulating of the wing by itself is very quick, as large timesteps or a prescribed wake can be used. The isolated propeller benefits tremendously from the axisymmetry of the problem, with only one blade and its wake requiring real panels, with the other five being represented by virtual panels [11]. The propeller-wing assembly requires more time, especially given the relatively small timestep needed for convergence results. However, the time of 8 hours, which corresponds to 160 CPU hours is orders of magnitude lower than the time required for an unsteady CFD simulation, which in the case of the LBM simulation referenced in this work cost $O(10000)$ CPU hours.

The times reported here can be reduced further in a number of ways. The setup can be optimized, to try to minimize the number of panels
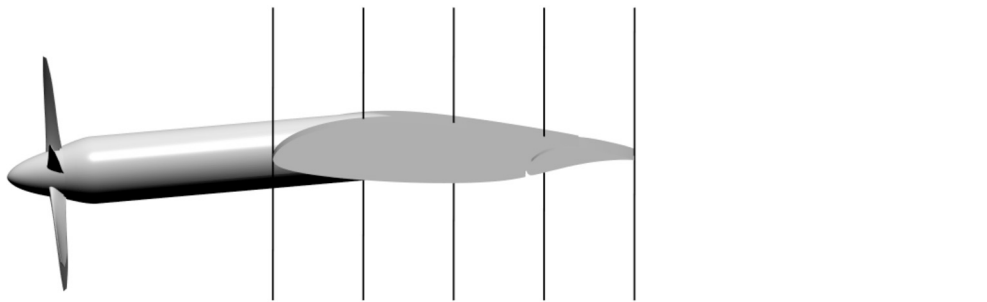
Fig. 13. Planes used throughout this section at $x/c = [0, 0.25, 0.5, 0.75, 1, 2]$.
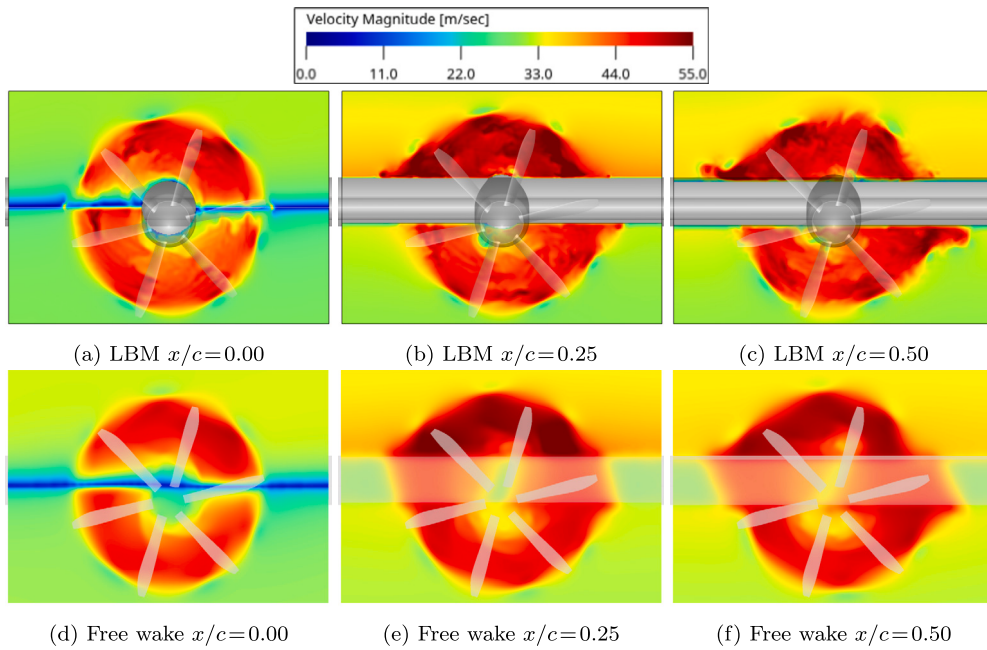

(a) LBM $x/c = 0.00$

(b) LBM $x/c = 0.25$

(c) LBM $x/c = 0.50$

(d) Free wake $x/c = 0.00$

(e) Free wake $x/c = 0.25$

(f) Free wake $x/c = 0.50$

Fig. 14. Velocity magnitude on planes along the slipstream. First half of the wing. Results using $\Delta\psi = 2.5°$.

(a) LBM $x/c = 0.75$

(b) LBM $x/c = 1.00$

(c) LBM $x/c = 2.00$

(d) Free wake $x/c = 0.75$
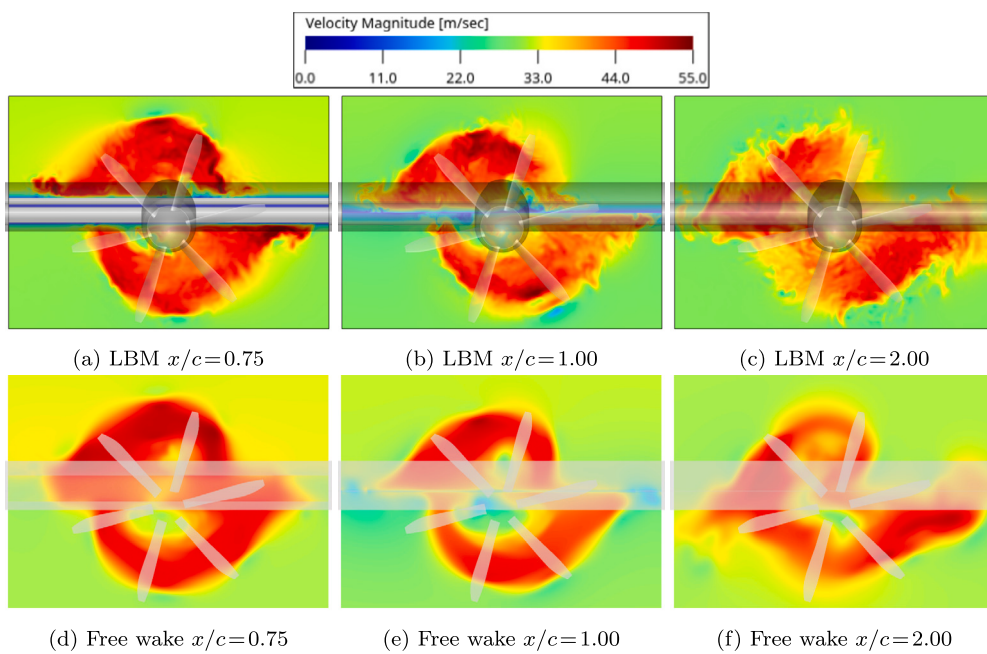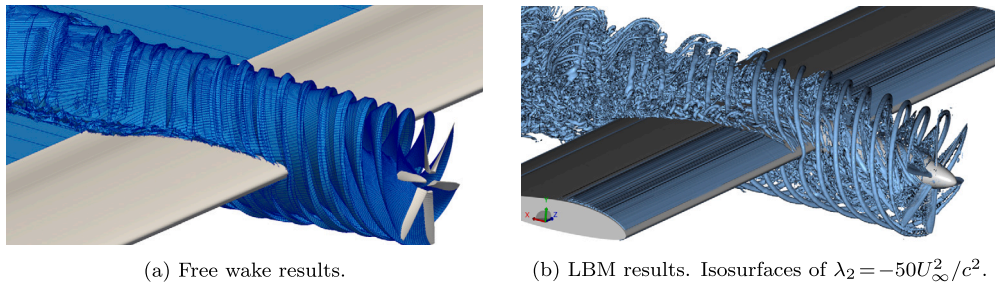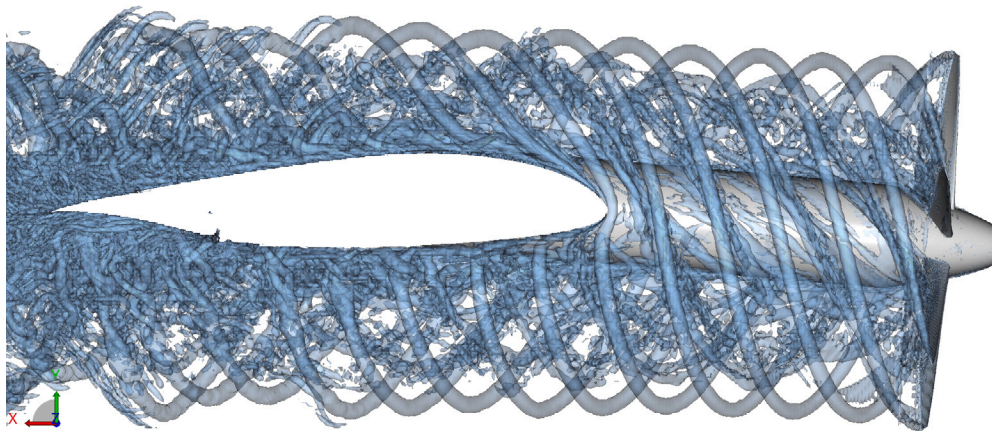
(e) Free wake $x/c = 1.00$

(f) Free wake $x/c = 2.00$

Fig. 15. Velocity magnitude on planes along the slipstream. Second half of the wing and downstream plane. Results using $\Delta\psi = 2.5°$.

(a) Free wake results.

(b) LBM results. Isosurfaces of $\lambda_2 = -50 U_\infty^2/c^2$.

Fig. 16. Visualisation of the slipstream deformation as it moves along the wing.

(a) Free wake results. Wake filaments penetrating through wing.

(b) LBM results. Isosurfaces of $\lambda_2 = -50 U_\infty^2/c^2$.

Fig. 17. Close-up view of slipstream going over the wing leading-edge. Wakes are shown with transparency, in order to see inside the slipstream.

Table 2

Approximate time required to perform each simulation on a desktop computer with 20 CPU cores and a GPU with 8 GB VRAM.

Case	Time	Notes
Wing	2 minutes	Prescribed wake or large timestep
Propeller	30 minutes	Axisymmetric, $\Delta\psi = 5°$
Propeller + Wing	8 hours	Mixed wake approach, $\Delta\psi = 5°$

used in the simulations. Further code optimization can be done to accelerate the computations. An obvious potential improvement is to skip the calculation of the flow velocity at all the wake points where the wake

is prescribed, which was not done in this work. Finally, more parts of the code could be performed on the GPU, as for the current simulations, only the computation of the wake velocities was performed on the GPU, as the linear system solution exceeded the GPU memory and other parts of the code were only written for CPUs.

6. Conclusions and outlook

In this work we employed lattice-Boltzmann simulations that were previously validated with experiments to evaluate the feasibility of using a filament-based free wake panel method for preliminary design of propeller-wing configurations. The experimental data was limited

to a few flow properties in certain locations and therefore the lattice-Boltzmann solution allowed for a detailed validation of the free wake simulations.

A mixed prescribed-free wake approach is used, with the wing wake being prescribed and the propeller wake free. This allowed for convecting the startup vortex away from the wing in few iterations, while keeping a small enough timestep to accurately model the propeller, and avoided issues with using the far wake formulation near the wing trailing-edge. Such mixed approach would have issues in a pusher configuration, but with a traditional upstream propeller, it was shown to be adequate, while changing the wing lift by less than 0.2%.

On the isolated propeller, the thrust obtained by the free wake simulations matched experimental data very well, while torque was not as accurate. This is expected, standing the inviscid nature of the free wake panel methodology, and has been seen before in wind turbines [34].

The force development on the wing showed that with a simple scaling of the forces, lift changes caused by the slipstream were well captured, while the pitching moment was less accurate and drag was inaccurate, as expected from an inviscid approach. Interestingly, the value for scaling the lift was selected to match the lift outside the slipstream and it seemed valid inside the slipstream as well. This means that a simple 2D XFOIL simulation can be used to estimate the scaling factor. The extend of the applicability of such scaling would need to be verified in a future study with more reference data. Such empirical scaling affects the reliability of such a method as a predictive tool, but is standard practice in aircraft design.

The pressure distribution showed that the small differences in viscous and inviscid isolated airfoil simulations become much larger in the presence of the slipstream, partially due to inaccuracies in angle of attack and flow velocity, but also because of underprediction of the slipstream shearing. Comparing the free wake pressure distribution closer to the propeller axis to reference data further away from the propeller axis led to very similar results. This means the free wake results need to be used with care, as relying on sectional forces without applying some sort of correction can lead to very overpredicted forces.

The propeller slipstream deformation as it traveled over the wing was remarkably similar to the reference simulations. There will always be differences when comparing to a scale-resolved simulation, with results appearing more smeared, but these wakes are relatively difficult and expensive to obtain with CFD. This could be the main use of a free wake method for eVTOL design: predicting and understanding wake interactions in complex configurations. The main shortcoming of the filament-based free wake approach here is the lack of vortex break-up and the upper and lower slipstreams always being connected, which is likely linked to the underprediction of the slipstream shearing.

The time required for the simulation of the propeller-wing assembly was two orders of magnitude faster than LBM, which could be suitable for preliminary design, but future work can be applied to accelerating the simulations further.

We believe that this work demonstrates that filament-based free wake panel code simulations are indeed able to provide some value in preliminary design phases of aircraft with propellers. There are severe limitations linked to the inviscid approach used in this work, but the method is also able to capture very complex flow physics which are generally difficult to capture. Future work can focus on extending the validation of the method, to verify the possibility of using simple corrections to account for viscous effects. More complex configurations can also be studied, such as multiple propellers, stability and control, as well as aeroelastic and aeroacoustic simulations.

Declaration of competing interest

The authors declare that they have no known competing financial interests or personal relationships that could have appeared to influence the work reported in this paper.

Data availability

Data will be made available on request.

References

[1] K.A. Deere, J.K. Viken, S. Viken, M.B. Carter, M. Wiese, N. Farr, Computational analysis of a wing designed for the X-57 distributed electric propulsion aircraft, in: 35th AIAA Applied Aerodynamics Conference, 2017.

[2] T. Sinnige, R. Nederlof, N. van Arnhem, Aerodynamic performance of wingtip-mounted propellers in tractor and pusher configuration, in: AIAA AVIATION FORUM, 2021.

[3] T.C.A. Stokkermans, D. Usai, T. Sinnige, L.L.M. Veldhuis, Aerodynamic interaction effects between propellers in typical evtol vehicle configurations, J. Aircr. 58 (4) (2021) 815–833, https://doi.org/10.2514/1.C035814.

[4] R. de Vries, N. van Arnhem, T. Sinnige, R. Vos, L.L. Veldhuis, Aerodynamic interaction between propellers of a distributed-propulsion system in forward flight, Aerosp. Sci. Technol. 118 (2021) 107009, https://doi.org/10.1016/j.ast.2021.107009.

[5] R.R. Duivenvoorden, N. Suard, T. Sinnige, L.L.M. Veldhuis, Experimental investigation of aerodynamic interactions of a wing with deployed fowler flap under influence of a propeller slipstream, in: AIAA AVIATION Forum, 2022.

[6] A.F.P. Ribeiro, R. Duivenvoorden, D. Martins, High-fidelity simulations of propeller-wing interactions in high-lift conditions, https://doi.org/10.2514/6.2023-3541, 2023.

[7] E. Branlard, Wind Turbine Aerodynamics and Vorticity-Based Methods, 1st edition, Research Topics in Wind Energy, Springer, 2017.

[8] M. Tugnoli, D. Montagnani, M. Syal, G. Droandi, A. Zanotti, Mid-fidelity approach to aerodynamic simulations of unconventional VTOL aircraft configurations, Aerosp. Sci. Technol. 115 (2021) 106804, https://doi.org/10.1016/j.ast.2021.106804.

[9] E.J. Alvarez, A. Ning, Modeling multirotor aerodynamic interactions through the vortex particle method, in: AIAA Aviation Forum, 2019.

[10] E.J. Alvarez, A. Ning, High-fidelity modeling of multirotor aerodynamic interactions for aircraft design, AIAA J. 58 (10) (2020) 4385–4400, https://doi.org/10.2514/1.J059178.

[11] J. Katz, A. Plotkin, Low-Speed Aerodynamics, 2nd edition, Cambridge Aerospace Series, Cambridge University Press, 2001.

[12] J.L. Hess, Panel methods in computational fluid dynamics, Annu. Rev. Fluid Mech. 22 (1) (1990) 255–274, https://doi.org/10.1146/annurev.fl.22.010190.001351.

[13] W. Johnson, Influence of wake models on calculated tiltrotor aerodynamics, in: American Helicopter Society Aerodynamics, Acoustics, and Test and Evaluation Technical Specialists' Meeting, 2002, https://rotorcraft.arc.nasa.gov/Publications/files/Johnson_AHS02.pdf.

[14] M. Gennaretti, G. Bernardini, Novel boundary integral formulation for blade-vortex interaction aerodynamics of helicopter rotors, AIAA J. 45 (6) (2007) 1169–1176, https://doi.org/10.2514/1.18383.

[15] G. Bernardini, J. Serafini, M. Molica Colella, M. Gennaretti, Analysis of a structural-aerodynamic fully-coupled formulation for aeroelastic response of rotorcraft, Aerosp. Sci. Technol. 29 (1) (2013) 175–184, https://doi.org/10.1016/j.ast.2013.03.002.

[16] B.M. Govindarajan, J.G. Leishman, Curvature corrections to improve the accuracy of free-vortex methods, J. Aircr. 53 (2) (2016) 378–386, https://doi.org/10.2514/1.C033392.

[17] V. Ahuja, B.L. Litherland, Comparison of aerodynamic analysis tools applied to a propeller-blown wing, in: AIAA SCITECH Forum, 2023.

[18] S. Succi, The Lattice Boltzmann Equation: For Fluid Dynamics and Beyond, Clarendon Press, 2001, https://books.google.com/books?id=OC0Sj_xgnhAC.

[19] E. Manoha, B. Caruelle, Summary of the LAGOON solutions from the benchmark problems for airframe noise computations-III workshop, in: 21st AIAA/CEAS Aeroacoustics Conference, 2015.

[20] V. Yakhot, S.A. Orszag, S. Thangam, T.B. Gatski, C.G. Speziale, Development of turbulence models for shear flows by a double expansion technique, Phys. Fluids A, Fluid Dyn. 4 (7) (1992) 1510–1520, https://doi.org/10.1063/1.858424.

[21] E. Fares, B. Duda, A.F.P. Ribeiro, B. König, Scale-resolving simulations using a lattice Boltzmann-based approach, CEAS Aeronaut. J. 9 (4) (2018), https://doi.org/10.1007/s13272-018-0317-0.

[22] M.R. Khorrami, B. Konig, E. Fares, A. Ribeiro, M. Czech, P.A. Ravetta, Airframe noise simulations of a full-scale large civil transport in landing configuration, in: AIAA AVIATION FORUM, 2021.

[23] H. Chen, C. Teixeira, K. Molvig, Realization of fluid boundary conditions via discrete Boltzmann dynamics, Int. J. Mod. Phys. C 09 (08) (1998) 1281–1292, https://doi.org/10.1142/S0129183198001151.

[24] R. Zhang, C. Sun, Y. Li, R. Satti, R. Shock, J. Hoch, H. Chen, Lattice Boltzmann approach for local reference frames, Commun. Comput. Phys. 9 (5) (2011) 1193–1205, https://doi.org/10.4208/cicp.021109.111110s.

[25] A.F.P. Ribeiro, Unsteady analysis of ground vortex ingestion with LBM-VLES, in: AIAA SCITECH Forum, 2021.

[26] G. Romani, D. Casalino, Rotorcraft blade-vortex interaction noise prediction using the lattice-Boltzmann method, Aerosp. Sci. Technol. 88 (2019) 147–157, https://doi.org/10.1016/j.ast.2019.03.029.

[27] D. Casalino, E. Grande, G. Romani, D. Ragni, F. Avallone, Definition of a benchmark for low Reynolds number propeller aeroacoustics, Aerosp. Sci. Technol. 113 (2021) 106707, https://doi.org/10.1016/j.ast.2021.106707.

[28] D. Casalino, W.C. van der Velden, G. Romani, A framework for multi-fidelity wind-turbine aeroacoustic simulations, in: 28th AIAA/CEAS Aeroacoustics 2022 Conference, 2022.

[29] D. Casalino, G. Romani, R. Zhang, H. Chen, Lattice-Boltzmann calculations of rotor aeroacoustics in transitional boundary layer regime, Aerosp. Sci. Technol. 130 (2022) 107953, https://doi.org/10.1016/j.ast.2022.107953.

[30] W. van der Velden, G. Romani, D. Casalino, Validation and insight of a full-scale S-76 helicopter rotor using the lattice-Boltzmann method, Aerosp. Sci. Technol. 118 (2021) 107007, https://doi.org/10.1016/j.ast.2021.107007.

[31] G. Romani, E. Grande, F. Avallone, D. Ragni, D. Casalino, Performance and noise prediction of low-Reynolds number propellers using the lattice-Boltzmann method, Aerosp. Sci. Technol. 125 (2022) 107086, https://doi.org/10.1016/j.ast.2021.107086, sI: DICUAM 2021.

[32] D. Casalino, G. Romani, L.M. Pil, R. Colombo, Sensitivity of laminar separation noise from a rotor to inflow turbulence, in: AIAA AVIATION Forum, 2023.

[33] S.D. Lucas-Bodas, J. Narbona-Gonzalez, V. Ossorio-Contreras, J. Jose Guerra-Crespo, D.E. Funes-Sebastian, L.P. Ruiz-Calavera, Experimental validation of numerical prediction of wing-propeller aerodynamic interaction, in: 32nd Congress of the International Council of the Aeronautical Sciences, 2021, https://www.icas.org/ICAS_ARCHIVE/ICAS2020/data/papers/ICAS2020_0171_paper.pdf.

[34] A.F.P. Ribeiro, D. Casalino, C.S. Ferreira, Surging wind turbine simulations with a free wake panel method, J. Phys. Conf. Ser. 2265 (4) (2022) 042027, https://doi.org/10.1088/1742-6596/2265/4/042027.

[35] A.F.P. Ribeiro, D. Casalino, C.S. Ferreira, Nonlinear inviscid aerodynamics of a wind turbine rotor in surge, sway, and yaw motions using a free-wake panel method, Wind Energy Sci. 8 (4) (2023) 661–675, https://doi.org/10.5194/wes-8-661-2023.

[36] A.F.P. Ribeiro, D. Casalino, C. Ferreira, Free wake panel method simulations of a highly flexible wing at flutter, in: AIAA AVIATION Forum, 2022.

[37] B. Maskew, Program vsaero theory document: a computer program for calculating nonlinear aerodynamic characteristics of arbitrary configurations, Contractor Report 4023, National Aeronautics and Space Administration, 1987, https://ntrs.nasa.gov/citations/19900004884.

[38] H. Youngren, E. Bouchard, R. Coopersmith, L. Miranda, Comparison of panel method formulations and its influence on the development of QUADPAN, an advanced low-order method, Appl. Aerodyn. Conf. (1983), https://doi.org/10.2514/6.1983-1827.

[39] M. Ramasamy, J.G. Leishman, A Reynolds number-based blade tip vortex model, J. Am. Helicopter Soc. 52 (3) (2007) 214–223, https://doi.org/10.4050/JAHS.52.214.

[40] W.K. Anderson, D.L. Bonhaus, An implicit upwind algorithm for computing turbulent flows on unstructured grids, Comput. Fluids 23 (1) (1994) 1–21, https://doi.org/10.1016/0045-7930(94)90023-X.

[41] E. Sozer, C. Brehm, C.C. Kiris, Gradient calculation methods on arbitrary polyhedral unstructured meshes for cell-centered CFD solvers, in: 52nd Aerospace Sciences Meeting, AIAA, 2014.

[42] J. Katz, D. Weihs, Hydrodynamic propulsion by large amplitude oscillation of an airfoil with chordwise flexibility, J. Fluid Mech. 88 (3) (1978) 485–497.

[43] L. Boermans, P. Rutten, Two-dimensional aerodynamic characteristics of airfoil NLF-MOD22 with fowler flap, Technical report, Delft University of Technology, 1995.

[44] N. van Arnhem, R. de Vries, T. Sinnige, L. Veldhuis, TUD-XPROP-S propeller geometry, https://doi.org/10.5281/zenodo.6355670, Mar. 2022.

[45] A.F.P. Ribeiro, D. Casalino, E. Fares, Lattice-Boltzmann simulations of an oscillating NACA0012 airfoil in dynamic stall, in: M. Braza, A. Bottaro, M. Thompson (Eds.), Advances in Fluid-Structure Interaction, Springer International Publishing, 2016, pp. 179–192.

[46] A.F.P. Ribeiro, D. Singh, B. Konig, E. Fares, On the stall characteristics of iced wings, in: 55th AIAA Aerospace Sciences Meeting, 2017.

[47] C.N. Sheridan, D.D. Pham, S. Whiteside, Evaluation of vspaero analysis capabilities for conceptual design of aircraft with propeller-blown wings, in: AIAA AVIATION FORUM, 2021.

[48] M. Drela, XFOIL: an analysis and design system for low Reynolds number airfoils, in: T.J. Mueller (Ed.), Low Reynolds Number Aerodynamics, Springer Berlin Heidelberg, Berlin, Heidelberg, 1989, pp. 1–12.